

High velocity steel spheres impact and damage analysis of graphene doped T700 composite shielding panels

Nelson Matos^{a,*}, Virginia Infante^b, Manuel Gomes^a, Mario Ribeiro^a, José Pedro Sousa^a,
Filipe Ribeiro^a, Ricardo Rocha^c

^a ISQ - Instituto de Soldadura e Qualidade, Av. Prof. Cavaco Silva, 2780 Porto Salvo, Portugal

^b LAETA, IDMEC, Instituto Superior Técnico, Universidade de Lisboa, Av. Rovisco Pais 1, 1049-001 Lisboa, Portugal

^c INEGI - Campus da FEUP, R. Dr. Roberto Frias 400, 4200-465 Porto, Portugal

ARTICLE INFO

Keywords:

Projectile impact
Metal projectile
Damage
Absorbed energy
Multilayer composite
T700
High velocity
Graphene

ABSTRACT

Composite materials are increasingly being used in aircraft components such as fuselage panels which are subject to collision with debris during take-off/landing or in flight. This article provides an analysis of the impact resistance capability of graphene doped T700 (T700G) multilayer composite, when subjected to steel projectile impacts. Test coupons with 300×300 mm were impacted by steel spherical projectiles, with impact energies ranging from 34 J to 338 J, using a compressed air operated cannon. Test data, such as impact and absorbed energy were determined through impact and residual projectile velocity, acquired using ballistic chronograph and two high speed cameras. Damage assessment was performed using non-destructive techniques such as Ultrasonic testing before and after impact test. Through modelling and simulation, using ABAQUS/Explicit, and recording the change of projectile velocity, the energy loss of projectile is calculated, and the impact resistance is judged together with damage extent. T700G has similar impact resistance to AL2024, underperforming when impacted by larger projectiles and presenting an overall higher damaged area.

Introduction

Several industrial sectors have been researching and developing composites as an alternative to traditional materials, due to their mechanical properties and lightweight. In sectors such as aeronautics, weight is of paramount importance in any structural optimization activity, which focus on improving functional performance while maintaining or reducing weight [1]. Composites have complex damage and failure mechanisms when subjected to impact phenomena, this being a critical factor to achieve a reliable and cost-effective alternative to traditional materials [2]. The most critical factor regarding composites damage is non-visible structural deterioration under the surface, which can occur in low (below 10 m/s), medium (10 to 50 m/s) or high-speed impacts (between 50 m/s and 1000 m/s) [3]. Impact damage can occur by several mechanisms such as matrix cracking, fibre/matrix de-bonding, fibre pull-out, delamination, and fibre breakage [1,4,5].

Moreover, since each layer of laminate behaves to impact in unique way, there are countless combinations of damage mechanisms [6]. Several impact studies have been performed addressing a wide variety of

composite materials and projectiles to determine the several mechanisms of kinetic energy dissipation as well as comprehensive overview papers of several experimental techniques for materials subjected to high velocity impact scenarios as the one from Pai et al. [7]. Rahimi et al. [8] have studied the influence of the different Kevlar and glass reinforced plastics (GRP) layout configurations and thicknesses, when impacted by different cylindro-conical projectiles, leading to the conclusion that fibre failure and local delamination are the main energy dissipation mechanisms. Carbon fibre-reinforced plastics (CFRPs) with various carbon fibres, with and without surface-treated fibres and polycrystalline graphite's, were subjected to impacts from spherical projectiles traveling between 150 and 1300 m/s. Results show that at the same impact velocities, maximum stress was largely dependent on the reinforcing fibres, whereas weak interfaces appear to lead to low stress and strain in CFRPs. When the stress rose above a specific level (dependent on the reinforcement fibre), polycrystalline graphite's had a significant impact on the stress and began to behave fluid-like. Xie et al. [9] found that the CFRP delamination zone of the subsequent layers is dispersed in a fan-shaped region, and the direction of the delamination is

* Corresponding author.

E-mail address: nelson.matos@ist.utl.pt (N. Matos).

<https://doi.org/10.1016/j.finmec.2024.100268>

Received 11 January 2024; Received in revised form 27 March 2024; Accepted 4 April 2024

Available online 4 April 2024

2666-3597/© 2024 The Authors. Published by Elsevier Ltd. This is an open access article under the CC BY-NC license (<http://creativecommons.org/licenses/by-nc/4.0/>).

Table 1

Coupons configuration and properties.

Ref.	Material	No. layers	Areal Density (kg/m ²)	Thickness (mm)	Layup
AL2024	AA 2024 T3	1	3.34	1.2	Not Applicable
T700G	T700+ Graphene	14	3.39	2.44	[45/−45/90/0/−45/45/0/0/45/−45/0/90/−45/45]

parallel to the direction of the fibres in the front ply and Liu et al. [10] identified, structural warpage, tension-shear failure associated to brittle fracture, spallation and punching perforation failure as the main failure modes. Thickness is also identified as one major parameter for impact energy absorption since it correlates directly with the capability of the material to absorb energy by elastic deformation of the laminate [11]. Frictional energy during penetration, arising from the laminate inertia, or back-face deformation, can also be correlated with thickness [12]. Projectile mass and velocity also influence the impact phenomena and was studied by Cantwell and Morton [3,13], determining that in carbon fibre reinforced polymers (CFRP) laminates, low velocity impact has a global panel deformation area, while with higher projectile velocity the relevant area for the impact phenomena is increasingly localized. Yuan et al. [14] researched the perforation resistance of laminated CFRP beam and square plate where the dynamic deformation, damage process, and resulting damage were captured in the specimens using high-speed photography and non-invasive damage detective techniques, together with numerical simulations using a constitutive model compiled through a VUMAT subroutine in ABAQUS.

The addition of graphene to CFRP has as one of its objectives the improvement of mechanical properties. Graphene is a honeycomb-shaped crystal lattice of tightly packed sp²-bonded carbon atoms that has a thickness equal to one carbon atom's atomic size [15]. Avila et al. [16] subjected to ballistic impacts several hybrid nanocomposites composed of different configurations of fiberglass/epoxy/nano-clay and fiberglass/epoxy/nano graphene and reported that nano-clay and graphene additions into the epoxy matrix increase the energy absorption capacity of the hybrid nano-composites. Moreover, [16] reported that the addition of nanoparticles of graphene and clay improved the energy absorption capacity of fibre reinforced epoxy composite. Nanoparticles were shown to increase penetration resistance by acting as a barrier to crack development and strengthening the link between the fibre and matrix. Graphene can enhance the functionality of the polymer obtaining superior mechanical behaviour against an external load as well as certain multifunctional qualities in electrical conductivity. For instance, Rafiee et al. [17] showed that the mechanical performance of Graphene nanoplatelets (GNPs) in epoxy matrix is superior to that of carbon nanotubes in terms of Young modulus, tensile strength, and buckling resistance. An additional in-depth analysis of multifunctional characteristics of graphene in composites can be found at [18].

To investigate the graphene doped T700 composite (T700G) impact performance, experimental studies were conducted using spherical steel projectiles with impact velocities ranging from 100 m/s to 200 m/s corresponding respectively to 34 J and 338 J. The analysis focused on the energy absorption and damage resistance of the T700G composite and an aluminium alloy material (AA2024 T3), which is currently implemented in operating aircrafts and will be the comparison baseline. Additionally, the composite material was mechanically characterised to determine the properties for the development of the simulation model. Simulations were then performed to determine the residual velocity, energy absorbed and damage area, and validated against experimental results.

Table 2

Mechanical properties of 2024-T3 aluminium alloy.

Young's Modulus	Yield Stress	Tensile strength	Poisson's ratio	Elongation
73.4 GPa	315 MPa	550MPa	0.33	0.18 %

Table 3

T700 12 K fibre properties.

Property	Value
Tensile strength	4900 MPa
Tensile Modulus	230 GPa
Strain at Failure	2.1 %
Density	1.80 g/cm ³
Tow size	12K
Filament Diameter	7µm
Yield	800 g / 1000 m
Chemical composition: Carbon	>93 %



Fig. 1. Impact experimental setup.

Materials

The tested materials (Table 1) consist of a hot rolled aluminium alloy 2024-T3 (AA2024-T3), 1.2 mm thick, as a benchmark solution (Table 2), and a composite material referenced as T700G (Table 3), which is a nano-filled matrix framed by UD T700 carbon fibres and MTC9800 (provided by SHD) – graphene enhanced epoxy resin, (MTC9800-UD140-T700–12K-40 % RW).

Test coupons were manufactured in a clean room designed and built for classification 10 K, ISO 7.

The vacuum bagging method was used to perform the laminate cure. A vacuum line was used to provide 1.0 bar, and the oven was heated to 80 °C with a ramp rate of 2 °C per minute. During curing, the autoclave pressure was maintained at 5 bars and the panels were cured for ten minutes at that temperature, then they were subjected to 1 hour curing cycle at 120°C before being cooled down to room temperature for a period of 1 hour with a similar ramp rate.

Metal spheres, used as projectiles, consisted of two diameters, 12 mm (7.05 gr.) and 19.05 mm (28.2 gr.). The steel spheres were supplied by a bearing manufacturer, and these are AISI 52,100 with a hardness of 57–66 HRC.

Experimental procedure

The experimental stage consists in striking the coupons using metal spheres, with velocities of 100 m/s, 150 m/s and 200 m/s. These velocities encompass typical take off speed and the 150 m/s cruise velocity



Fig. 2. Compressed air cannon.



Fig. 3. Target holder.



Fig. 4. Velocity measurement setup.

of regional turboprop aircraft, as defined by EASA CS-25 [19] for debris impact. The experimental setup for the high velocity impact tests (Fig. 1) consists of a pressurized gas cannon (Fig. 2) which propels the projectile, using a foam sabot, through a 108 mm internal diameter smooth bore



Fig. 5. Phased array inspections - Immersion tank.

Table 4

Mechanical properties of unidirectional T700G laminate.

Standard	Properties	Value
ASTM D3039 [36]	Tensile strength f_{11t} (MPa)	1577.10
	Tensile modulus E_{11t} (MPa)	95,248.23
	Poisson Coef. ν_{12}	0.319
	Tensile strength f_{22t} (MPa)	37.14
	Tensile modulus E_{22t} (MPa)	7370.70
ASTM D6641 [37]	Compressive strength f_{11c} (MPa)	–
	Compressive modulus E_{11c} (MPa)	19,058.90
	Compressive strength f_{22c} (MPa)	22.43
	Compressive modulus E_{22c} (MPa)	1613.25
	In-plane shear strength f_{12su} (MPa)	140.15
ASTM D3518 [38]	In-plane shear modulus G_{12s} (MPa)	2904.39
EN 2563 [39]	Interlaminar shear strength f_{13} (MPa)	70.50
ASTM D5528 [40]	Interlaminar fracture toughness energy - mode I G_{IC} (kJ/m ²)	0.100
ASTM D7905 [41]	Interlaminar fracture toughness energy - mode II G_{IIC} (kJ/m ²)	2.514
In-house method	Longitudinal tensile fracture toughness G_{xt} (kJ/m ²)	115.37
In-house method	Longitudinal compressive fracture toughness G_{xc} (kJ/m ²)	21.74

barrel. The $300 \times 300 \text{ mm}^2$ coupons (exposing a $240 \times 240 \text{ mm}^2$ area) are installed in a target holder (Fig. 3), composed by two steel plates firmly connected to a steel portico ensuring a perpendicular position to the firing axis of the cannon.

The velocity measurement setup (Fig. 4) is composed of two high velocity cameras (Photron AX200, Photron SA5) and a ballistic chronograph (Caldwell G2), allowing to determine both the impact and residual projectile velocity.

Damage assessment of non-metallic solutions is performed using immersion tank (Fig. 5) and PAUT (Phased Array Ultrasonic Testing) [20–22], while for metal coupons radiography was used. PAUT was performed using an M2M MultiX ++ model together with IMASONIC (4 MHz – 60 elts model) and OLYMPUS (5 MHz – 128 elements model) probes. X-ray was carried out using a YXLON (ANDREX) Smart YXLON model.

Composites impact resistance performance was determined by analysing the damage area and absorbed energy. Several measurements and calculated variables were considered, namely: impact and residual velocity (determined by chronograph and high velocity cameras); projectile impact energy, absorbed energy; and damage area (visual inspection and non-destructive testing techniques detailed above) – including measurement of delamination [23,24].

Impact and absorbed energy were calculated using the below for-

mulas:

$$E_{\text{impact}} = \frac{1}{2} m_p v_{\text{impact}}^2 \quad (1)$$

$$E_{\text{absorbed}} = \frac{1}{2} m_p (v_{\text{impact}}^2 - v_{\text{residual}}^2) \quad (2)$$

Where E_{impact} is the impact energy in [J], m_p is the projectile mass in [kg], v_{impact} is the impact velocity of the projectile in [m/s], E_{absorbed} is the impact energy absorbed by the specimen in [J], v_{residual} is the residual velocity of the projectile in [m/s].

T700G was mechanically characterized to obtain all relevant material properties for the numerical simulation model, the properties and applicable standards are presented in Table 4.

Mechanical characterization campaign was performed at room temperature (21°C) using the following equipment and instrumentation:

- INSTRON 4208 fitted with a 30 kN load cell
- INSTRON 8800 fitted with a 250 kN load cell
- INSTRON 8562 fitted with a 30 kN load cell
- Strain gauge HBM 1-XY91-3/120 (120ohm resistance)
- Strain gauge HBM 1-LY11-3/120 (120ohm resistance)

Numerical simulation approach

The numerical simulation was focused from the point of view of energy absorption and composite damage on the scope of high velocity impact test simulations. Numerical simulations in the present study were conducted employing the Abaqus/explicit solver.

Materials models

The material response of aluminium and steel was assumed to be isotropic elastic-plastic with isotropic hardening. The available isotropic plasticity model in Abaqus was adopted, with employing the Johnson-Cook isotropic hardening [25,26]. The static yield stress, σ^0 , is assumed to have the form

$$\sigma^0 = [A + B(\bar{\epsilon}^{\text{pl}})^n](1 - \hat{\theta}^m) \quad (3)$$

Where $\bar{\epsilon}^{\text{pl}}$ is the equivalent plastic deformation, $\hat{\theta}^m$ is the nondimensional temperature and A, B, n and m are material parameters measured at or below the transition temperature, $\theta_{\text{transition}}$.

With respect to the Johnson-Cook strain rate dependence it is assumed that

$$\bar{\sigma} = \sigma^0(\bar{\epsilon}^{\text{pl}}, \theta) R(\dot{\epsilon}^{\text{pl}}) \quad (4)$$

and

$$\dot{\epsilon}^{\text{pl}} = \dot{\epsilon}_0 \exp \left[\frac{1}{C} (R - 1) \right] \text{ for } \bar{\sigma} \geq \sigma^0 \quad (5)$$

Where $\bar{\sigma}$ is the yield stress at a non-zero strain rate, $\dot{\epsilon}^{\text{pl}}$ is the equivalent plastic strain rate; $\dot{\epsilon}_0$ and C are material parameters measured at or below the transition temperature, $\theta_{\text{transition}}$; $\sigma^0(\bar{\epsilon}^{\text{pl}}, \theta)$ is the static yield stress, and $R(\dot{\epsilon}^{\text{pl}})$ is the ratio between the yield stress at a non-zero strain rate and the static yield stress (so that $R(\dot{\epsilon}_0) = 1.0$).

In the current model, the T700G was modelled as an orthotropic material, and the damage initiation, or the beginning of deterioration, was based on the Hashin's theory [27]. Abaqus library also contains this degradation criterion [28]. According to Hashin, an ideal failure criterion for unidirectional fibre reinforced polymer composites is the one that can distinguish between the several failure modes and model each one separately. The identification of each failure mode, still according to

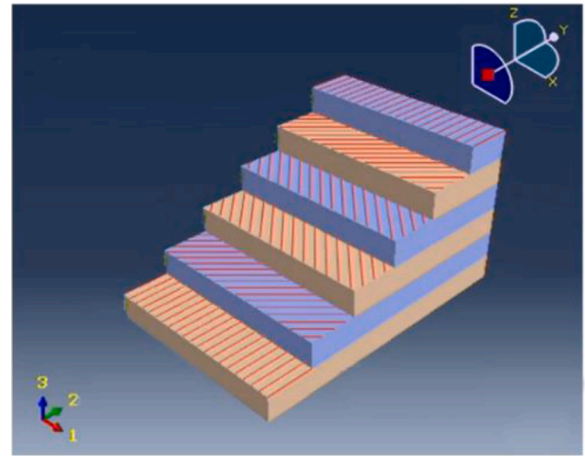


Fig. 6. First 6 layers of stacked shells with different fibre orientation.

Hashin, is indispensable for modelling the damage propagation, confirmed by Coelho et al. [29] who found Hashin's criterion was accurate enough for predicting the fibre-tension dominated failures in composite laminates.

In Hashin's criterion, the severity of the tensile stress in the fibre direction is predicted by the following expression [27].

$$f_f^t = \left(\frac{\sigma_1}{X_t} \right)^2 + \left(\frac{\sigma_{12}}{S_\sigma} \right)^2, \sigma_1 \geq 0 \quad (6)$$

In the case of compression in the direction of the fibres, failure is predicted by a different condition:

$$f_f^c = \left(\frac{-\sigma_1}{X_c} \right), \sigma_1 < 0 \quad (7)$$

In the case of a transverse tensile stress, possibly with shear, the expression to predict matrix failure is:

$$f_m^t = \left(\frac{\sigma_2}{Y_t} \right)^2 + \left(\frac{\sigma_{12}}{S_\sigma} \right)^2, \sigma_2 \geq 0 \quad (8)$$

And when the transverse solicitation is compression, a slightly more complete expression is used:

$$f_m^c = \left(\frac{\sigma_2}{2S_\sigma} \right)^2 + \left(\frac{\sigma_{12}}{S_\sigma} \right)^2 + \left[\left(\frac{Y_c}{2S_\sigma} \right)^2 - 1 \right] \frac{\sigma_2}{Y_c}, \sigma_2 < 0 \quad (9)$$

Finally, the one that is most severe for the loading in question is selected from one of the previous modes:

$$f = \max(f_f^t, f_f^c, f_m^t, f_m^c) \quad (10)$$

Whereas in the case of non-phenomenological criteria, generally take the form of polynomials, in particular quadratic ones. Considering a plane state of stress, the polynomial is of the following form:

$$f = F_{11}\sigma_1^2 + F_{22}\sigma_2^2 + F_{66}\sigma_{12}^2 + 2F_{12}\sigma_1\sigma_2 + F_1\sigma_1 + F_2\sigma_2 + F_6\sigma_{12} \quad (11)$$

The coefficients F_{ij} and F_i are determined so that the failure criterion function is equal to 1 when a unidirectional stress state corresponding to the failure stress of the material is installed.

Simulation modelling

The aluminium panels were discretized with eight-node linear brick solid elements with reduced integration (C3D8R), while steel spheres projectiles used 4-node linear tetrahedral element (C3D4). The T700G was modelled using the 8-node, quadrilateral, first-order interpolation, stress/displacement continuum shell element with reduced integration

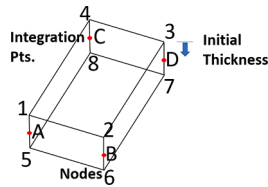


Fig. 7. COH3D8 cohesive element.

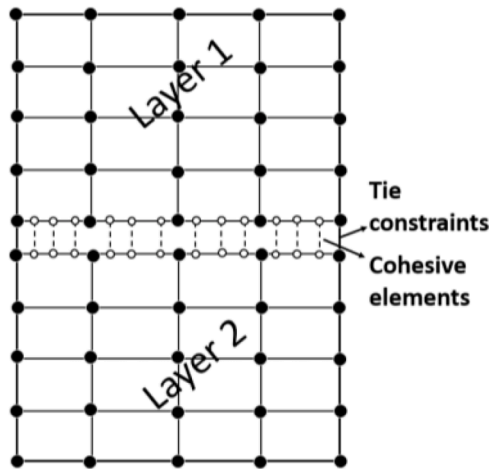


Fig. 8. Cohesive mesh.

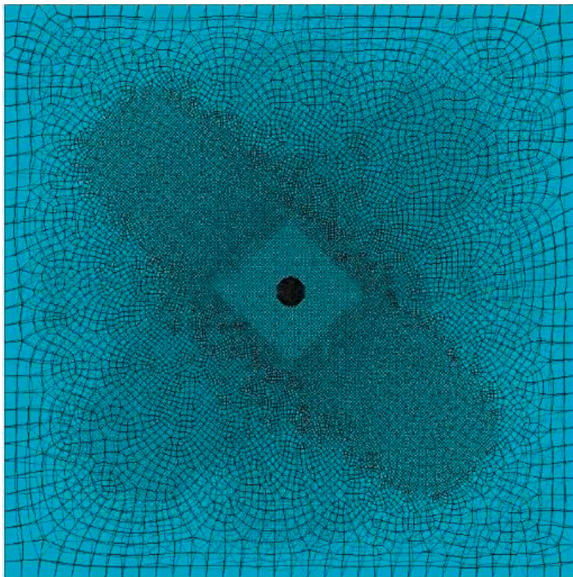


Fig. 9. T700G mesh.

(SC8R). The use of stacked shells method (Fig. 6), where each shell has its unique fibre orientation, allowed for the capture of the onset delamination between layers.

Interply cohesion was modelled with eight-node three-dimensional cohesive elements (COH3D8). The two virtual surfaces (Fig. 7) for crack propagation, are the surface defined by nodes 1–2–3–4 and the surface defined by nodes 5–6–7–8. The two surfaces of the cohesive elements separate from one another under the effect of the applied load, and the relationship between traction load and separation complies with the specified fundamentals [30].

Additionally interface cohesive layers meshing followed the best practices to have a very refined mesh in the cohesive zone but also

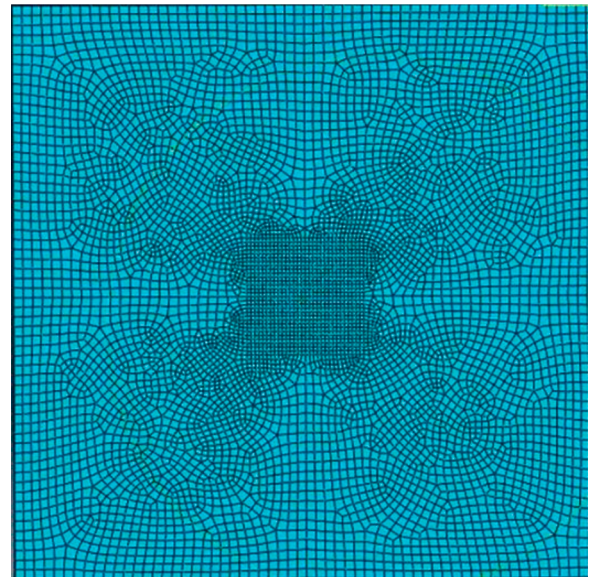


Fig. 10. AL2024 mesh.

considering the computational costs (Fig. 8). Several studies have been performed regarding the optimal mesh size and number of cohesive connections [31,32]. Considering previous investigations, a 0.15 mm mesh size was defined according to [33] thus ensuring enough cohesive elements in the cohesive zone.

Aluminium panel was meshed with a central refined mesh area of two times the largest projectile diameter, while T700G had two main mesh areas. A cross shape area with a finer mesh was defined in the direction of the 45° fibre direction, following the recommendation that the mesh should be parallel to the fibres to accurately simulate damage propagations within the fibres. Rajaneesh et al. [34] developed high velocity impact carbon fibre reinforced polymeric laminates models, for explicit dynamic analyses, using orthotropic material aligned mesh together with Bazant-type crack-band/smeared-crack formulation mesh size regularization and element erosion. Developed models were validated by comparing with test data and numerical results from the literature. Away from this zone, a coarse mesh was used with the objective of reducing the computation effort. The different mesh densities described are depicted in Fig. 9 and Fig. 10.

Mesh element size in both aluminium and T700G layers was determined based on the mesh sensitivity analysis regarding the calculation of projectile residual velocity.

The intermediate impact velocity of 150 m/s was chosen for this analysis and 0.75 mm element size was defined for the most refined mesh zone, (Fig. 11). The free mesh zone has a compromised coarse mesh to reduce computational times.

According to the target holder solution used in the impact tests (Fig. 3), where the targets are firmly clamped between two steel plates, a fully fixed boundary condition was selected.

Steel spheres projectiles were meshed using 10,026 linear tetrahedral elements of type C3D4 for the Ø19 mm and 10,112 elements for the Ø12 mm. Mechanical properties wise, a density of 7800 kg/m³, a Young Modulus of 210 GPa and a Poisson coefficient of 0.3, were used to parametrize the projectiles.

Results and discussion

Mechanical characterization

The campaign of mechanical tests described in Section 3, allowed to obtain the mechanical properties of T700G composite (Table 4) and build the numerical simulation model. For aluminium 2024-T3

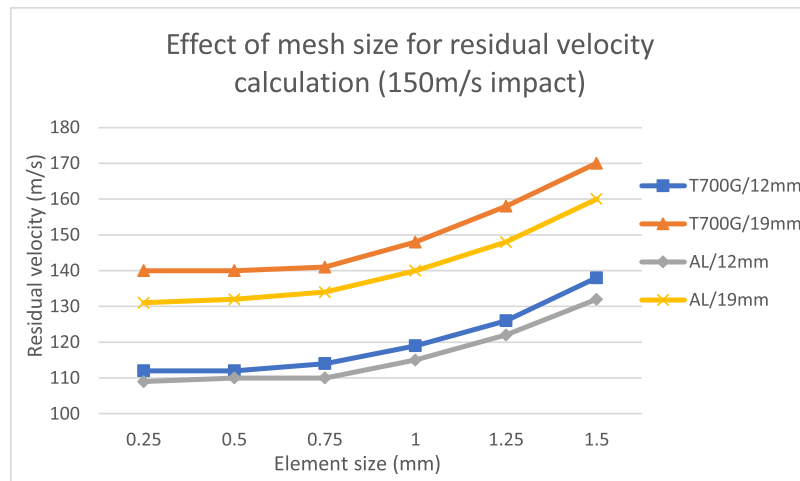


Fig. 11. Effect of mesh size for residual velocity calculation (150 m/s impact).

Table 5

Impact tests and velocity details of T700G and AL2024.

Steel Sphere		Velocity [m/s]			Steel Sphere		Velocity [m/s]		
Diam. (mm)		Impact	Residual	Residual sim.	Diam. (mm)		Impact	Residual	Residual sim.
Al_1	12	99.0	-8.8	-8.2	T700G_1	12	97	-9.1	-8.3
Al_2	12	148.0	115.1	110.2	T700G_2	12	101	-10.7	-7.9
Al_3	12	149.0	109.3	110.8	T700G_3	12	109	42.0	42.5
Al_4	12	149.0	115.8	110.8	T700G_4	12	149	115.0	115.2
Al_5	12	198.0	176.0	174.5	T700G_5	12	150	117.4	119.9
Al_6	19.05	89.0	-7.2	-5.1	T700G_6	12	190	169.8	172.6
Al_7	19.05	97.0	11.6	10.5	T700G_7	12	204	175.0	173.3
Al_8	19.05	103.0	46.4	46.0	T700G_8	19.05	94	65.0	65.4
Al_9	19.05	155.0	134.3	134.9	T700G_9	19.05	101	74.6	86.3
					T700G_10	19.05	151	141.4	141.3
					T700G_11	19.05	155	141.0	142.5

modelling, material properties were retrieved from [35].

Impact testing

Twenty impact tests were performed, eleven on the T700G and the remaining nine on the AL2024. The projectiles impact velocities, residual velocities and simulated residual velocities are presented in Table 5.

Impact velocities were as close as possible to 100, 150 and 200 m/s to ensure a consistent basis for comparisons. The rebound velocities were determined using the high-speed images but due to the projectile trajectory not being totally perpendicular to the camera, some error is admissible.

Both T700G and AL2024 resisted perforation with the Ø12 mm projectile, however with very low rebound velocities indicating that they were at the limit of their impact resistance or ballistic limit –

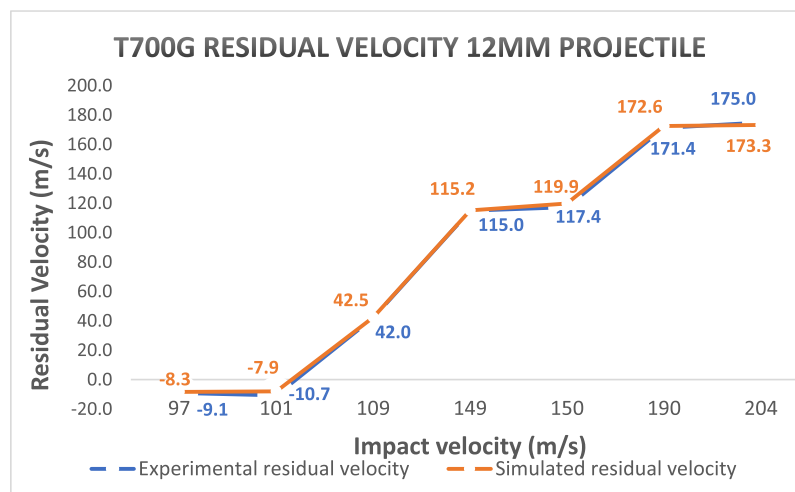


Fig. 12. T700G residual velocity (experimental and simulated) with Ø12 mm projectile.

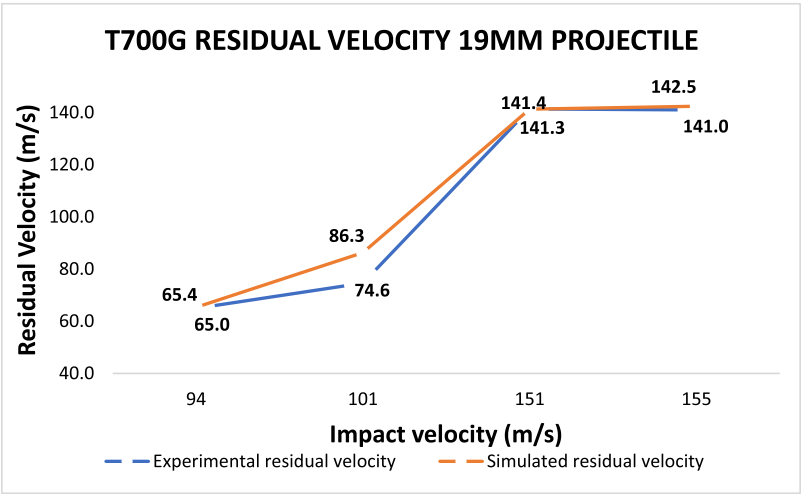


Fig. 13. T700G residual velocity (experimental and simulated) with Ø19 mm projectile.

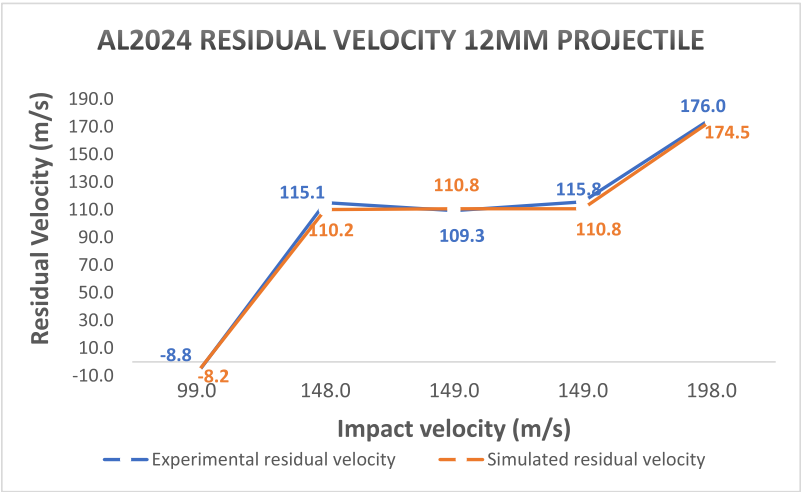


Fig. 14. AL2024 residual velocity (experimental and simulated) with Ø12 mm projectile.

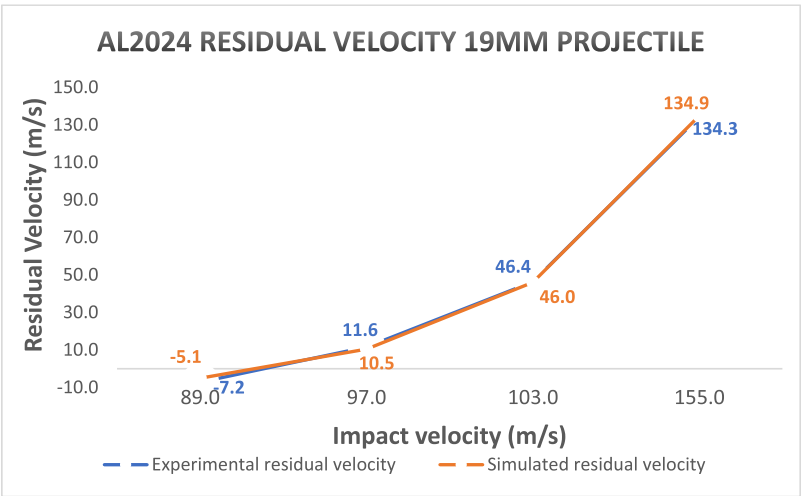


Fig. 15. AL2024 residual velocity (experimental and simulated) with Ø19 mm projectile.

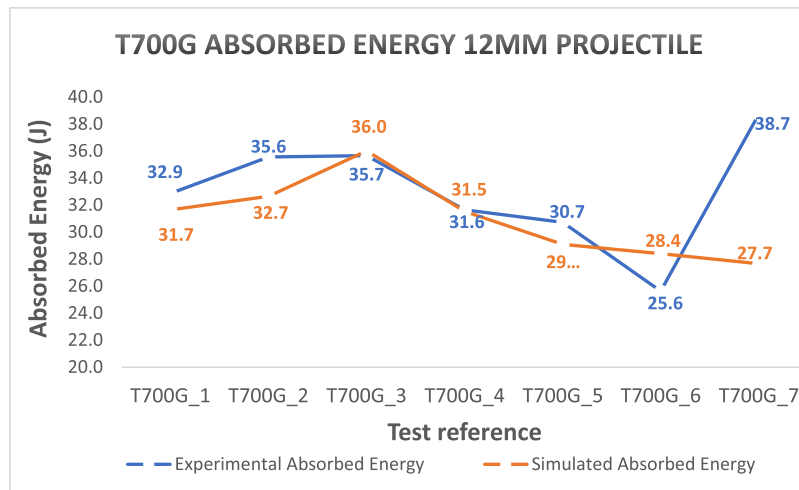


Fig. 16. T700G absorbed energy (experimental and simulated) with Ø12 mm projectile.

around 100 m/s. Effectively it can be observed that in the T700G_3 test, the increase in about 8 m/s above the velocity of T700G_2, led to the perforation of the target. Additionally, AL2024_6 was able to resist perforation with the Ø19 mm projectile at 89 m/s, again with a low rebound velocity. The next trial, AL2024_7 impacted at 97 m/s managed to pierce the target. Target perforation was confirmed in all T700G targets when impacted with Ø19 mm, independently of the impact velocity.

As expected, the residual velocities of the Ø19 mm projectile were much higher than those of the Ø12 mm projectile because mass enhances penetration and holds more kinetic energy. Even though the maximum contact area is greater, its impact energy is higher as well, as the sectional density in the Ø12 mm projectile is two and a half times smaller than on the Ø19 mm projectile.

Simulation comparison with experimental results

To validate the numerical simulations, typical experimental and numerical comparison were carried out, encompassing the residual velocity, energy absorbed and target damage area.

Residual velocity

Fig. 12, 13, 14, Fig. 15, based on Table 5 data, depict the residual velocity for each test performed using the Ø12mm and Ø19 mm

projectiles. Note that all speeds tested are represented on the graphs and therefore the horizontal sections do not represent an increased resistance to perforation of the material with increasing speed.

It is easily identifiable the perforation resistance plateau up to the impact velocity of 100 m/s, being afterwards registered an increase of the residual velocity of the projectile with similar slope until 200 m/s. With the increase of the impact velocity is also visible an approximation of the residual velocity values to the impact velocity. At 109 m/s, near the ballistic limit, the residual velocity is about 40 % of the impact velocity, while around 200 m/s it increases to 85 %. Additionally, a good agreement was obtained between the experimental and simulation results.

A similar phenomenon exists with the impacts using the Ø19 mm projectiles. The simulation has a good correlation with the experimental results although in the impact at 101 m/s, both the simulation and experimental values, if aligned with the impact values of 94 m/s and 151 m/s, suggest there should be a higher residual velocity than the one recorded.

When impacting with heavier Ø19 mm projectiles it is also noted that the residual velocities are much closer to the impact velocities, with values in the 150 m/s range between 90 and 95 %.

Regarding the impacts performed on AL2024, the behaviour recorded is quite like the T700G profile. The simulation model replicates quite faithfully the experimental events and obtains a higher correlation than with the T700G. With Ø12 mm projectiles, the behaviour is

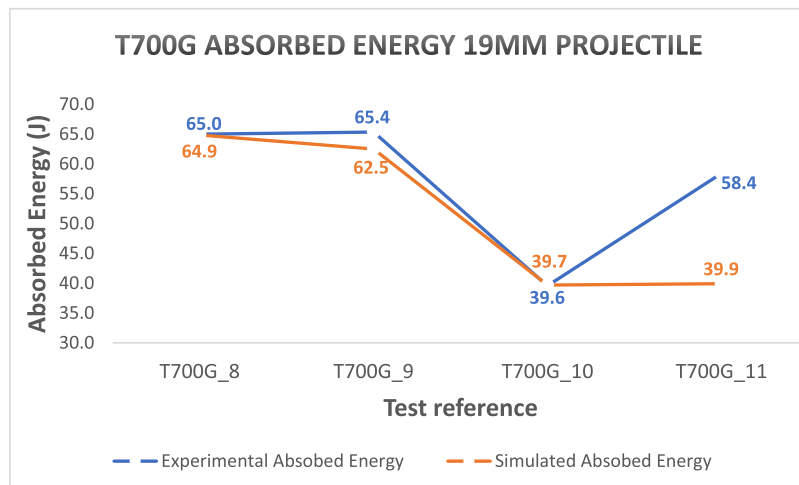


Fig. 17. T700G absorbed energy (experimental and simulated) with Ø19 mm projectile.

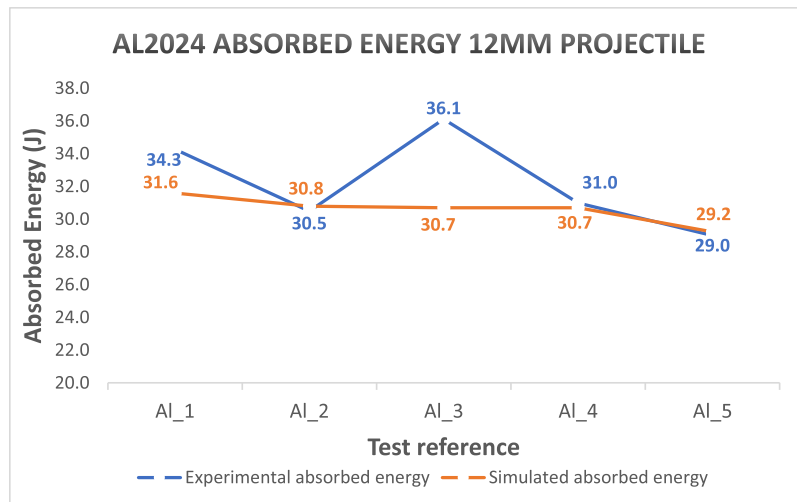


Fig. 18. AL2024 absorbed energy (experimental and simulated) with Ø12 mm projectile.

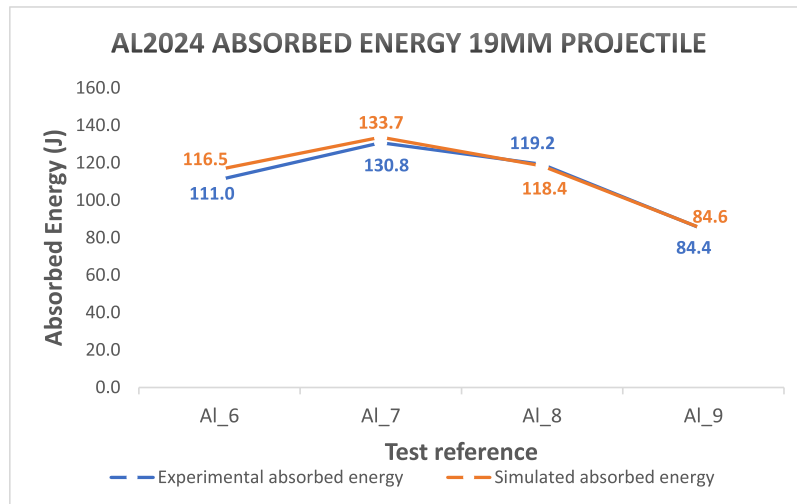


Fig. 19. AL2024 absorbed energy (experimental and simulated) with Ø19 mm projectile.

identical to the T700G, including the relationship between the residual velocity and the impact velocity, a situation that changes when analysing the behaviour with Ø19 mm projectiles. The most relevant aspect of the impact with Ø19 mm projectiles is the ability of AL2024 to resist perforation at 89 m/s and have a very low residual velocity of 11.6 m/s when impacted at 97 m/s, especially compared with the 65 m/s residual velocity of the T700G impacted at 94 m/s.

Energy absorption

Figs. 16–19 depict the impact energy absorption for each test performed using the Ø12 mm and Ø19 mm projectiles. T700G impact energy absorption with Ø12 mm projectiles trended in a very similar way to the residual velocity. It can be observed a peak in the energy value in T700G_3 which is the test nearest to the ballistic limit. Previous impacts although non-perforating also have lower impact energy and remaining tests tend to have lower energy absorption, in line with the higher residual velocities.

Outside this behaviour is T700G_7, which presented a much higher than expected absorbed energy value because of the deviation of the previously calculated residual velocity to 204 m/s (Fig. 16). Since the procedure and equipment remained unchanged during all the tests it can only be assumed that there was some manufacturing deviation in the

panel that justifies this discrepancy. Homogenous dispersion of graphene in epoxy plays a very crucial role in the improvement of the mechanical properties, influencing the loads to filler material transfer effectiveness.

The T700G behaviour with Ø19 mm projectiles is quite like that described for the previous case. AL2024 tests demonstrated once again that the highest value of absorbed energy is found in the test with the impact velocity closest to the ballistic limit. In the tests with Ø12 mm projectiles, the maximum value of absorbed energy corresponds to Al_3.

The small deviation in residual velocity computed for Al_3 (Fig. 18) becomes very relevant in terms of absorbed energy. This does not seem to invalidate the similar trends between the experimental and the numerical results. However, the values obtained for Al_2, Al_4 are very close, so that the result for Al_3 should be disregarded. This way, the peak energy is found in Al_1 whose residual velocity is a rebound one, with a very low value, confirming the trend.

In the tests using Ø19 mm projectiles (Fig. 19), no anomalous values were recorded. The peak of absorbed energy is identifiable in Al_7, whose ballistic limit is close to the impact velocity of this reference (97 m/s). The remaining tests show a slight decrease of the absorbed energy in line with the increase of the impact velocity.

In both cases the numerical simulation presented good agreement with experimental results.

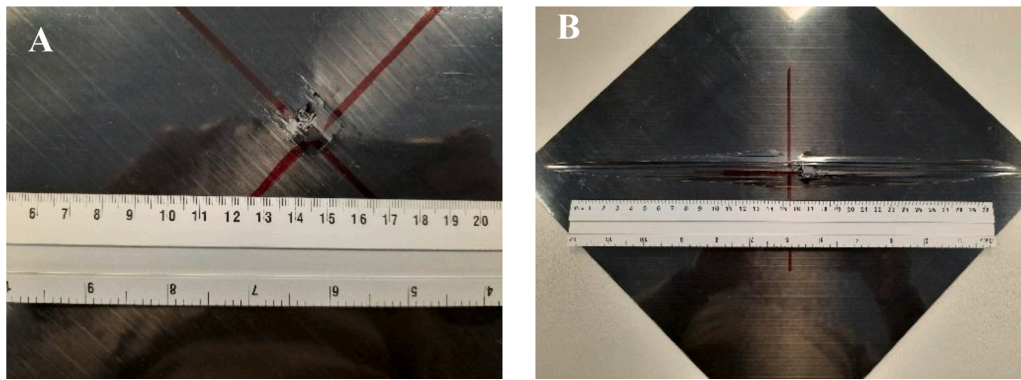


Fig. 20. T700G_6 target after impact. Front side (A) and back side (B). Note: Coupon rotated 45°.

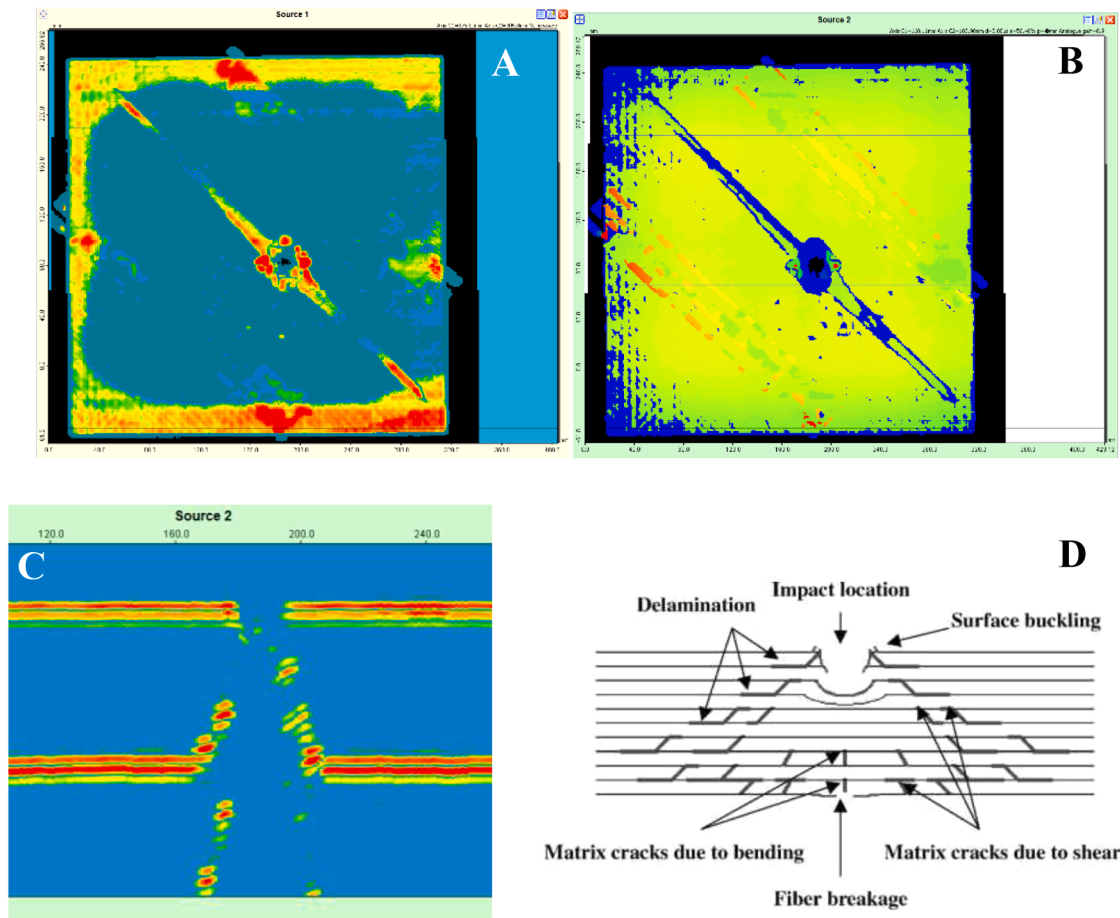


Fig. 21. NDT results of T700G_6. C-Scan with colour scale in amplitude (A) and in time (B). Cutaway view of the entire length of the plate (C). Typical impact damage for laminated composite [42] (D).

Damage area

The damage extension analysis was performed using visual techniques and non-destructive inspection techniques such as ultrasonic testing and X-ray, respectively for T700G and AL2024.

The visible damage was analysed, and the internal damage of each target was estimated. Other measurements such as the crater size were also performed to allow a more in-depth comparison with the simulation results for the AL2024.

T700G presented an almost perfect entry hole in contrast with the exit hole where extensive delamination had occurred. This can be seen in Fig. 20B, where the damage to the back of the coupon extends almost

from one vertex to the other, in the 45° direction.

At the forward face of the coupon, the projectile's superior kinetic energy led to the rupture of the fibres, and upon target penetration there was a loss of kinetic energy leading to its deceleration. As the projectile exited the back face it did not possess sufficient energy to overcome the resistance of the fibres, hence the structural failure of the composite is assigned to the matrix, allowing the sphere to pass between the fibres and causing extensive delamination without fibre rupture.

The PAUT captured the internal extent of the damage and allowed its quantification in detail. Apart from the obvious fibre breakage there is extensive damage around the entrance hole (Fig. 21A&B). It is also possible to observe that the severity of the delamination is correctly

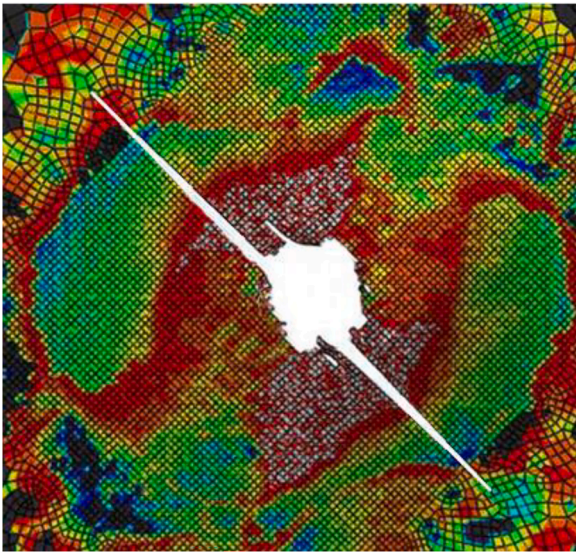


Fig. 22. T700G_6 damaged area simulation.

characterised by the fibres.

In Fig. 21C, it is possible to see a cone-shaped damage, with a reduced diameter damaged area at the front face and with increasing of damaged area along the thickness, as expected for laminated composite damage (Fig. 21D) [42]. Regarding T700G damage simulation, results are in line with what was expected. Simulations were able to identify the delamination surrounding the impact location as well as the damage that was aligned with the fibres (Fig. 22). The numerical simulations did not fully replicate the delamination that can be seen on the back face of the plate. However, in terms of residual velocity and absorbed energy, this does not appear to have a significant impact.

Despite the model's good residual velocity accuracy, the damaged area was poorly represented. Below and at the T700G_3 ballistic limit (100 m/s), the model's accuracy starts to decline (Fig. 23).

Damage simulation for the Ø19 mm impacts also presented a similar deviation as for Ø12 mm. T700G_11 (Fig. 24) also presented a result quite inconsistent with the simulation, but that is related and in line with what was discussed above regarding the absorbed energy for this coupon.

The perforated AL2024 coupons showed minor dishing deformation, following the petal damage pattern, with visible cracks (Fig. 25 and Fig. 26). In some of the coupons there was clogging and mass loss through ejection of small volumes of aluminium (Fig. 27).

In all test coupons, the X-ray did not detect any additional defects

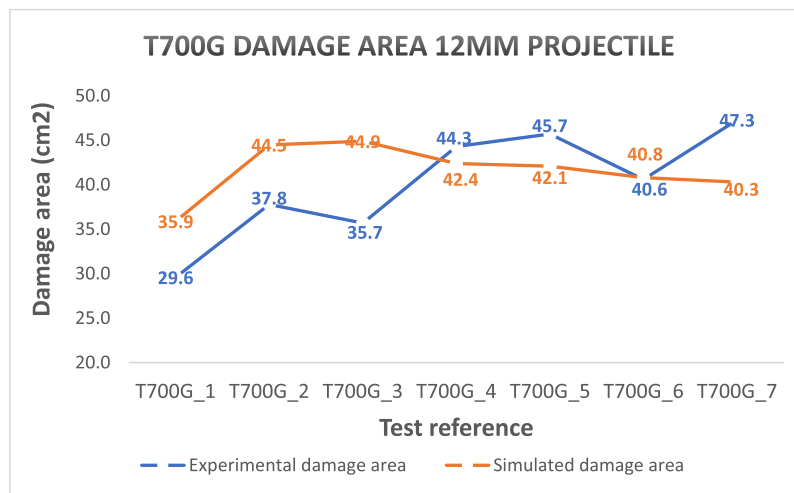


Fig. 23. T700G damage area (experimental and simulated) with Ø12 mm projectile.

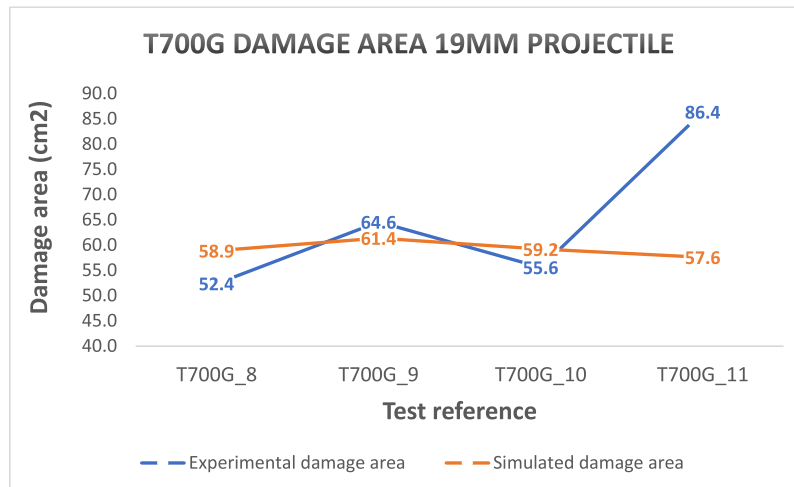


Fig. 24. T700G damage area (experimental and simulated) with Ø19 mm projectile.

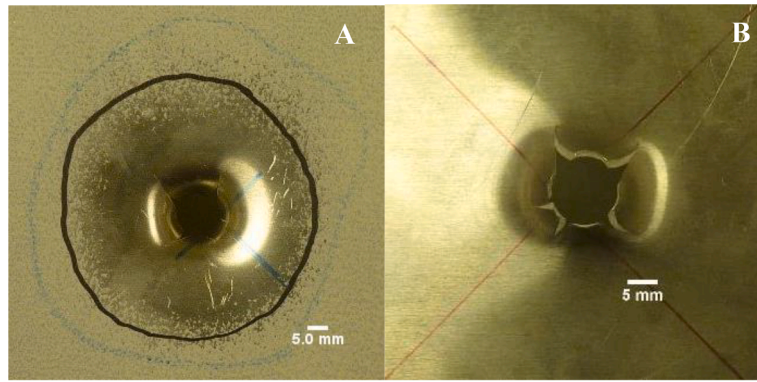


Fig. 25. Al₂ (12 mm @100 m/s) target after impact. Front side (A) and back side (B).

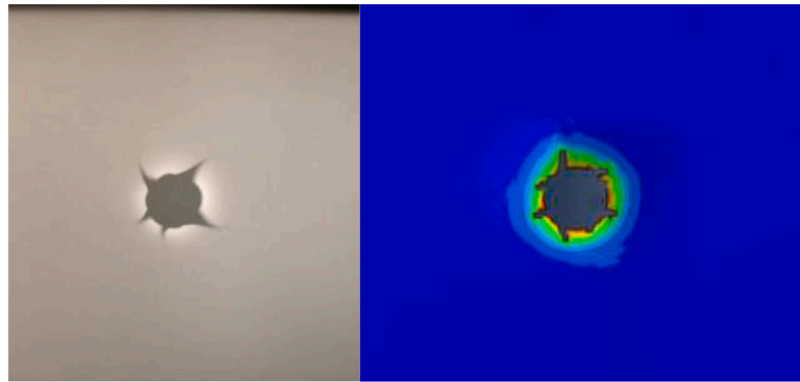


Fig. 26. X-ray results and damaged area simulation of Al₂.

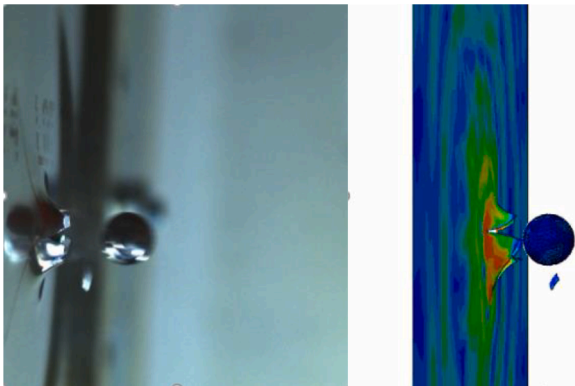


Fig. 27. Side view of experimental and simulated impact (AL2024 target).

other than the visual ones (Fig. 26).

For the aluminium 2024-T3 the simulations were able to capture the experimental behaviour. Fig. 25 and Fig. 26, allow for comparison between the numerical plastic deformed area and experimental results (for the Al₂ that was tested with the 12 mm metal sphere at 148 m/s). Small deviations were found in Al₂ for both the residual velocities and the absorbed energy, thus the shape of the damage is also very similar, with a representative small deformation around the hole caused by the plugging effect.

Fig. 27 demonstrates that the simulation was even able to reproduce the ejection of an aluminium fragment during the impact event.

Fig. 28 and Fig. 29 compare the experimental and numerical damaged area for the AL2024. The experimental damaged area was measured with digital image analysis. The depicted aluminium coupons

damaged area deviations were caused by dishing deformation of the coupon; however, the simulated damage area profile is well correlated with the experimental one. Additionally, the model accurately predicts the petal deformation geometry.

Since there is a relevant discrepancy between the experimental and simulated damage values, the authors also chose to compare crater diameter (Table 6).

The crater diameter simulation results are very close to the experimental results and thus obtaining good overall agreement between simulation and experimental results.

Impact performance comparison between T700G and AL2024

The main objective in keeping the same areal density of T700G as the AL2024, is to allow an almost direct comparison of results. However, since it was not possible to perform all impacts at the exact same velocities to compare the performance of T700G to the one of AL2024, it was decided to calculate the ratio between the values of absorbed energy and damage in function of impact energy. A simple average of the absorbed energy and damage ratios was made for each of the 3 foreseen impact velocities (100, 150 and 200 m/s). The representation can be found in Fig. 30 and Fig. 31.

Concerning the energy absorbed with Ø12 mm projectiles, there is a very similar performance between AL2024 and T700G at 100 m/s, while at 150 m/s there is a slight advantage for AL2024. This situation inverts with the increase of the impact speed, registering at 200 m/s a slightly better impact energy absorption capability by the T700G. In relation to damage, the results are highly enlightening, indicating that the T700G always presented greater areas of damage at any speed.

In impacts with Ø19 mm projectiles, AL2024 presented a higher impact energy absorption performance than T700G at both velocities, but if at 100 m/s it presented a larger damaged area, at 150 m/s the

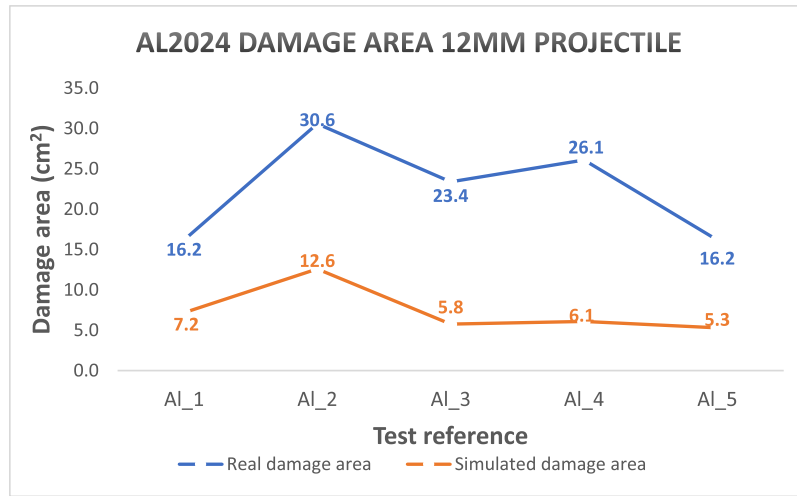


Fig. 28. AL2024 damage area (experimental and simulated) with Ø12 mm projectile.

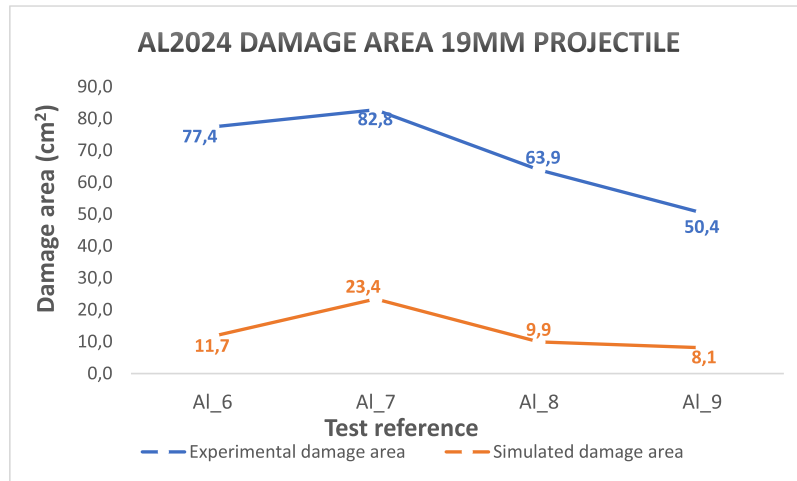


Fig. 29. AL2024 damage area (experimental and simulated) with Ø19 mm projectile.

Table 6

AL2024 crater diameter after impact.

		Al_1	Al_2	Al_3	Al_4	Al_5	Al_6	Al_7	Al_8	Al_9
Crater diameter [mm]	Measured	na	10.7	12.1	10.7	10.9	na	25.6	14.8	13.9
	Simulated	na	10.6	10.9	10.9	11.4	na	21.6	15.4	12.6

situation was the inverse.

One of the explanations for a higher damage ratio at 100 m/s is related to the fact that Al_6 resisted the perforation and Al_7 was very close to the ballistic limit which translated into a higher absorbed energy at the expense of a bigger damage area. Moreover, it is also observable that the absorbed energy value of AL2024 is almost twice of T700G.

Aluminium and T700G absorb energy in different ways. Because of its ductility, aluminium flexes when struck, absorbing impact energy and dispersing it over a wider region. T700G is less prone to this kind of deformation because of its greater rigidity. It is not as successful as AL2024 at absorbing and dissipating impact energy without breaking.

In comparison to AL2024, T700G is more brittle due to its matrix material which is less able to bend without breaking, while the fibres themselves have a high tensile strength. This indicates that AL2024, which is more ductile, can absorb impact energy through plastic deformation without failing, but T700G is more prone to crack or shatter when subjected to large impact forces, as seen in the back faces of the

panels.

T700G graphene absorption mechanisms are based on its ability to be simultaneously rigid, resistant, and elastic, stretching in a cone shape due to the force transmitted by the projectile. This stiffness and elasticity are provided by the high aspect ratio, meaning that these properties cover a large area, distributing the tension more effectively through the epoxy matrix. The kinetic energy of a projectile when it hits an impact point must be immediately redistributed through the layer perpendicular to the direction of impact, turning the point impact into a surface impact [43]. Effective load transfer between graphene and the epoxy matrix is achieved through strong covalent bonds within the graphene network, ensuring that applied forces are distributed throughout the composite material, avoiding localized stress concentrations and potential failure points.

Sadegh [44] demonstrated that besides the number of layers/thickness, the impact resistance of a graphene structure is significantly influenced by the ratio between width and height, distance between

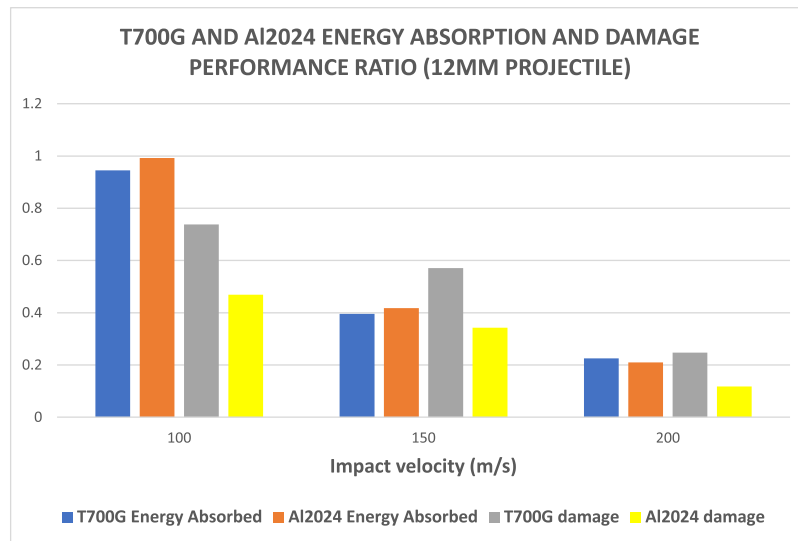


Fig. 30. T700G and AL024 energy absorption and damage performance ratio ($\varnothing 12$ mm projectile).

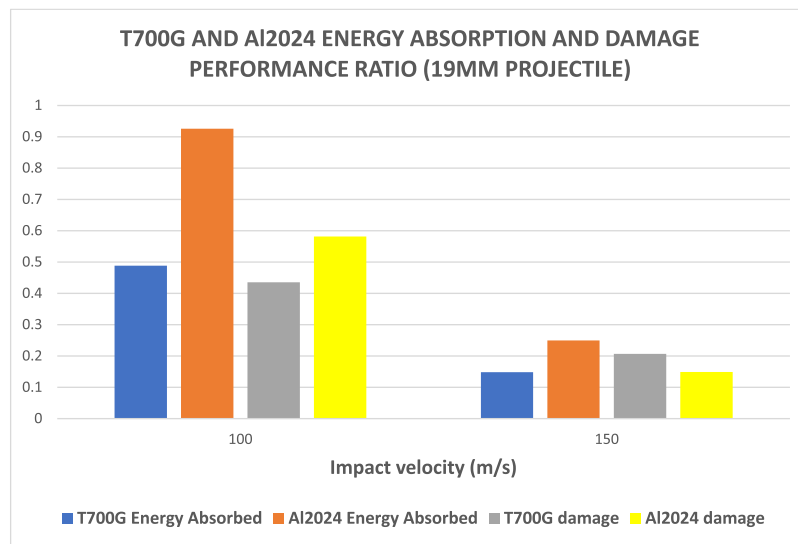


Fig. 31. T700G and AL024 energy absorption and damage performance ratio ($\varnothing 19$ mm projectile).

layers, and the force profile applied and its concentration, which are very specific for the impact of a rigid projectile. A rigid projectile impact stresses the material in a very localized and severe way diminishing the ability of the mechanisms described above to work efficiently. Aymerich [45] also concluded in his research through various experimental tests that the effect of adding graphene to epoxy matrices is more relevant for the absorbed energy than for the peak force which suggests that this functionalization of matrices with graphene is more appropriate for soft body impacts.

Additionally, Cuvillo et al. [46] identified that both the homogeneity of graphene dispersion and the dispersed amount have a significant influence on the composite's performance. Experimental results from mechanical tests on a CFRP with a graphene-enhanced matrix showed that mechanical properties were improved by about 6 % with a 0.8% wt addition, while 0.4% wt and 1.2% wt demonstrated inferior performance. The percentage of graphene addition used in MTC9800 may not be the most suitable for this type of impact and forces involved.

Conclusions

Impact tests and numerical simulation were performed to characterise the behaviour of T700G to metallic sphere impacts and to compare with the currently baseline material in usage, AL2024. Three aspects were evaluated (residual projectile velocity, impact energy absorbed by the material and damaged area) to determine the impact resistance and validate the numerical simulation models.

The conclusions are drawn as follows:

- The performance of both materials, for the tested thickness, is quite similar with slight advantage for AL2024, although it is possible to further optimize the T700G composite structure and its multifunctional properties may represent an added value even in face of a slight lower impact resistance performance.
- AL2024 shows a higher capacity to resist the penetration and reduce the projectile velocity, especially for bigger projectiles. This is a fact evident from the absorbed energy data.

- The damaged area of the AL2024 was lower than the T700G in most coupons, only presenting bigger damage area when was capable of resisting penetration.
- The combined action of compressive and shear loads primarily causes fibre breakage, matrix crushing, and splitting along the fibre direction on the impact face of the T700G target plate. Tensile loads are the main cause of fibre fracture and delamination failure on the target plate's back face where fibre breakage and pull-out, along the 45° direction can be found.
- Epoxy graphene doping in the T700 did not transfer more efficiently the external loads through polymer/filler interfacial interactions. The effectiveness of loads being transferred to the epoxy matrix is greatly influenced by percentage and homogenous dispersion of graphene, which can be a subject of future study and development.
- Good agreement was found between the impact testing and numerical simulation, however the software's element elimination feature, respective mass erosion and removal of strain energy from the structure can be potential causes for the less good correlation between experimental and simulation data of the T700G.

CRediT authorship contribution statement

Nelson Matos: Writing – original draft, Validation, Investigation, Formal analysis. **Virginia Infante:** Writing – review & editing, Supervision. **Manuel Gomes:** Validation, Supervision, Investigation. **Mario Ribeiro:** Supervision, Validation. **José Pedro Sousa:** Investigation. **Filipe Ribeiro:** Validation, Investigation. **Ricardo Rocha:** Validation, Investigation.

Declaration of competing interest

The authors declare the following financial interests/personal relationships which may be considered as potential competing interests:

Nelson Matos reports administrative support and writing assistance were provided by Técnico Lisboa Department of Mechanical Engineering.

Data availability

Data will be made available on request.

Acknowledgment

This work was funded by European funds under the Portuguese National Programme Portugal 2020, project MOSHO - LISBOA-01-0247-FEDER-033796 and supported by FCT, through IDMEC, under LAETA project UID/EMS/50022/2020.

References

- [1] N. Razali, M. Sultan, F. Mustapha, N. Yidris, M. Ishak, Impact damage on composite structures - a review, *Int. J. Eng. Sci. (IJES)* 3 (2014) 08–20.
- [2] A. Misra, *Composite materials for aerospace propulsion related to air and space transportation. Lightweight Composite Structures in Transport*, Elsevier, 2016, pp. 305–327, <https://doi.org/10.1016/B978-1-78242-325-6.00012-8>.
- [3] W.J. Cantwell, J. Morton, Comparison of the low and high velocity impact response of CFRP, *Composites* 20 (1989) 545–551, [https://doi.org/10.1016/0010-4361\(89\)90913-0](https://doi.org/10.1016/0010-4361(89)90913-0).
- [4] Z. Wang, M. Zhao, K. Liu, K. Yuan, J. He, Experimental analysis and prediction of CFRP delamination caused by ice impact, *Eng. Fract. Mech.* 273 (2022) 108757, <https://doi.org/10.1016/j.engfractmech.2022.108757>.
- [5] G. Zhou, Damage mechanisms in composite laminates impacted by a flat-ended impactor, *Compos. Sci. Technol.* 54 (1995) 267–273, [https://doi.org/10.1016/0266-3538\(95\)80019-0](https://doi.org/10.1016/0266-3538(95)80019-0).
- [6] A. Malhotra, F.J. Guild, Impact damage to composite laminates: effect of impact location, *Appl. Compos. Mater. (Dordr)* 21 (2014) 165–177, <https://doi.org/10.1007/s10443-013-9382-z>.
- [7] A. Pai, M. Rodriguez-Millan, M. Beppu, B. Valverde-Marcos, S.S. B, Experimental techniques for performance evaluation of shielding materials and configurations subjected to Blast and Ballistic impacts: a State-of-the-Art Review, *Thin-Walled Structures* 191 (2023) 111067, <https://doi.org/10.1016/j.tws.2023.111067>.
- [8] H. Rahimi, M.H. Beheshty, A.R. Sabet, High velocity impact of glass-reinforced plastic laminates with sharp nose projectile experimental results versus some models predictions, *Mech. Adv. Mater. Struct.* 22 (2015) 521–529, <https://doi.org/10.1080/15376494.2012.749317>.
- [9] W. Xie, W. Zhang, H. Yang, H. Wei, L. Wang, Y. Gao, X. Cai, Experimental investigation of high velocity impact response of CFRP laminates subjected to flyer plate impact, *Thin-Walled Struct.* 178 (2022) 109521, <https://doi.org/10.1016/j.tws.2022.109521>.
- [10] Q. Liu, B. Guo, P. Chen, J. Su, A. Arab, G. Ding, G. Yan, H. Jiang, F. Guo, Investigating ballistic resistance of CFRP/polyurea composite plates subjected to ballistic impact, *Thin-Walled Structures* 166 (2021) 108111, <https://doi.org/10.1016/j.tws.2021.108111>.
- [11] S.K. García-Castillo, S. Sánchez-Sáez, E. Barbero, Influence of areal density on the energy absorbed by thin composite plates subjected to high-velocity impacts, *J. Strain Anal. Eng. Design* 47 (2012) 444–452, <https://doi.org/10.1177/0309324712454996>.
- [12] S.S. Morye, P.J. Hine, R.A. Duckett, D.J. Carr, I.M. Ward, Modelling of the energy absorption by polymer composites upon ballistic impact, *Compos. Sci. Technol.* 60 (2000) 2631–2642, [https://doi.org/10.1016/S0266-3538\(00\)00139-1](https://doi.org/10.1016/S0266-3538(00)00139-1).
- [13] W.J. Cantwell, J. Morton, The influence of varying projectile mass on the impact response of CFRP, *Compos. Struct.* 13 (1989) 101–114, [https://doi.org/10.1016/0263-8223\(89\)90048-2](https://doi.org/10.1016/0263-8223(89)90048-2).
- [14] K. Yuan, K. Liu, Z. Wang, M. Yang, An investigation on the perforation resistance of laminated CFRP beam and square plate, *Int. J. Impact. Eng.* 157 (2021) 103967, <https://doi.org/10.1016/J.IJIMPENG.2021.103967>.
- [15] S. Park, R.S. Ruoff, Chemical methods for the production of graphenes, *Nat. Nanotechnol.* 4 (2009) 217–224, <https://doi.org/10.1038/nnano.2009.58>.
- [16] A.F. Ávila, A.S. Neto, H. Nascimento Junior, Hybrid nanocomposites for mid-range ballistic protection, *Int. J. Impact. Eng.* 38 (2011) 669–676, <https://doi.org/10.1016/j.ijimpeng.2011.03.002>.
- [17] M.A. Rafiee, J. Rafiee, Z. Wang, H. Song, Z.-Z. Yu, N. Koratkar, Enhanced mechanical properties of nanocomposites at low graphene content, *ACS. Nano* 3 (2009) 3884–3890, <https://doi.org/10.1021/nn9010472>.
- [18] R. Atif, I. Shyha, F. Inam, Mechanical, thermal, and electrical properties of graphene-epoxy nanocomposites—a review, *Polymers. (Basel)* 8 (2016) 281, <https://doi.org/10.3390/polym8080281>.
- [19] EASA, CS-25 certification specifications for large aeroplanes - amendment 27, (2023).
- [20] OmniScan MX2 Phased Array Flaw Detector, (n.d.). <https://www.olympus-ims.com/en/omniscan-mx2/> (accessed May 28, 2023).
- [21] H. Taheri, K.M. Ladd, F. Delfanian, J. Du, Phased Array Ultrasonic Technique Parametric Evaluation for Composite Materials, in: *Vibration, Acoustics and Wave Propagation*, 13, American Society of Mechanical Engineers, 2014, <https://doi.org/10.1115/IMECE2014-36945>.
- [22] M. Saadefar, M.A. Najafabadi, D. Zarouchas, H.H. Toudeshky, M. Jalalvand, Barely visible impact damage assessment in laminated composites using acoustic emission, *Compos. B Eng.* 152 (2018) 180–192, <https://doi.org/10.1016/j.compositesb.2018.07.016>.
- [23] B.M. Ganesh, R. Velmurugan, N.K. Gupta, Energy absorption and ballistic limit of targets struck by heavy projectile, *Latin Am. J. Solids Struct.* 3 (2006) 21–39.
- [24] ASTM D7136 /D7136M-20, Standard Test Method for Measuring the Damage Resistance of a Fiber-Reinforced Polymer Matrix Composite to a Drop-Weight Impact Event, ASTM International, 2020.
- [25] L. Antoinat, R. Kubler, G. Achard, J.L. Barou, V. Phlippe, L. Barralier, Low velocity perforation of an aluminum alloy: experiments and simulations, 3th International Conference on Fracture, ICF (2013), 42774–2753.
- [26] H. Ijaz, M. Zain-ul-abdein, W. Saleem, M. Asad, T. Mabrouki, Modified Johnson-Cook plasticity model with damage evolution: application to turning simulation of 2XXX aluminium alloy, *J. Mech.* 33 (2017) 777–788, <https://doi.org/10.1017/jmech.2017.11>.
- [27] Z. Hashin, Failure Criteria for Unidirectional Fiber Composites, *J. Appl. Mech.* 47 (1980) 329–334, <https://doi.org/10.1115/1.3153664>.
- [28] ABAQUS Version 6.6 Documentation, (n.d.). <https://classes.engineering.wustl.edu/2009/spring/mase5513/abaqus/docs/v6.6/index.html> (accessed May 28, 2023).
- [29] A.M. Girão Coelho, J. Toby Mottram, K.A. Harries, Finite element guidelines for simulation of fibre-tension dominated failures in composite materials validated by case studies, *Compos. Struct.* 126 (2015) 299–313, <https://doi.org/10.1016/j.compstruct.2015.02.071>.
- [30] H. Jiang, X. Gao, T.S. Srivatsan, A cohesive zone model for studying crack growth in materials and structures, *Neural, Parallel and Scientific Computations* 18 (3–4) (2010) 291–306. Authors Haodan Jiang University of Akron Xiaosheng Gao University of Akron T. S. Srivatsan University of Akron 18291–306.
- [31] R. Russo, B. Chen, Overcoming the cohesive zone limit in composites delamination: modeling with slender structural elements and higher-order adaptive integration, *Int. J. Numer. Methods Eng.* 121 (2020) 5511–5545, <https://doi.org/10.1002/nme.6497>.
- [32] P. Liu, Implicit Finite Element Analysis of Failure Behaviors of Adhesive Composite Joints Using Exponential and Bilinear Cohesive Models, *Damage Modeling of Composite Structures*, 2021, pp. 27–48, <https://doi.org/10.1016/B978-0-12-820963-9.00008-0>.
- [33] Q. Yang, B. Cox, Cohesive models for damage evolution in laminated composites, *Int. J. Fract.* 133 (2005) 107–137, <https://doi.org/10.1007/s10704-005-4729-6>.
- [34] A. Rajaneesh, J.P. Ponthot, M. Bruyneel, High velocity impact response of composite laminates using modified meso-scale damage models, *Int. J. Impact. Eng.* 147 (2021) 103701, <https://doi.org/10.1016/J.IJIMPENG.2020.103701>.

- [35] Aluminum 2024-T3, (n.d.). <https://www.matweb.com/search/DataSheet.aspx?MatGUID=57483b4d782940faaf12964a1821fb61&ckck=1> (accessed May 28, 2023).
- [36] ASTM International, ASTM, D3039/D3039M-08. Standard test method for tensile properties of polymer matrix composite materials, (2017).
- [37] ASTM International, ASTM, D6641/D6641M-09. Standard test method for compressive properties of polymer matrix composite materials using a combined loading compression (CLC) test fixture, (2021).
- [38] ASTM International, ASTM D3518/D3518M-18 standard test method for in-plane shear response of polymer matrix composite materials by tensile test of a $\pm 45^\circ$ Laminate, (2018).
- [39] ASTM International, ASTM D 2344 short-beam strength, (2022).
- [40] ASTM International, ASTM D5528/D5528M-21 standard test method for mode I interlaminar fracture toughness of unidirectional fiber-reinforced polymer matrix composites, (2022).
- [41] ASTM International, ASTM D7905/D7905M-19e1 standard test method for determination of the mode II interlaminar fracture toughness of unidirectional fiber-reinforced polymer matrix composites, (2019).
- [42] A. Maier, R. Schmidt, B. Oswald-Tranta, R. Schledjewski, Non-destructive thermography analysis of impact damage on large-scale CFRP automotive parts, *Materials*. (Basel) 7 (2014) 413–429, <https://doi.org/10.3390/MA7010413>, 2014, Vol. 7, Pages 413–429.
- [43] W. Xie, J.-H. Lee, Intrinsic dynamics and toughening mechanism of multilayer graphene upon microbullet impact, *ACS. Appl. Nano Mater.* 3 (2020) 9185–9191, <https://doi.org/10.1021/acsanm.0c01267>.
- [44] S. Sadeghzadeh, Computational design of graphene sheets for withstanding the impact of ultrafast projectiles, *J. Mol. Graph. Model.* 70 (2016) 196–211, <https://doi.org/10.1016/j.jmgm.2016.10.001>.
- [45] F. Aymerich, A.D. Via, M. Quaresimin, Energy absorption capability of nanomodified glass/epoxy laminates, *Procedia Eng.* 10 (2011) 780–785, <https://doi.org/10.1016/j.proeng.2011.04.129>.
- [46] R. del Cuvillo, J.A. Artero-Guerrero, J. Pernas-Sánchez, J. López-Puente, Impact performance on industrial scalable graphene reinforcement composites, *Aerosp. Sci. Technol.* 141 (2023) 108480, <https://doi.org/10.1016/j.ast.2023.108480>.